IEEE Photonics Journal
An IEEE Photonics Society Publication

Photonic Microcantilevers With Interferometric Bragg Grating Interrogation

Volume 4, Number 5, October 2012

Lewis G. Carpenter
Christopher Holmes
Benjamin D. Snow
James C. Gates
Peter G. R. Smith

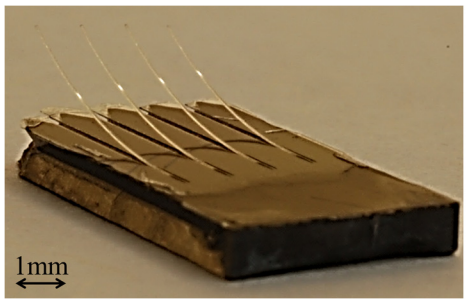

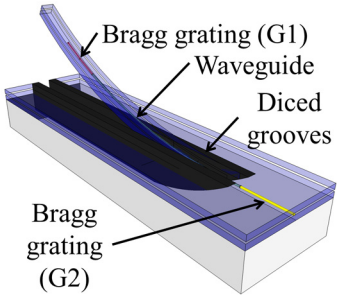

DOI: 10.1109/JPHOT.2012.2210396
1943-0655/$31.00 ©2012 IEEE

Photonic Microcantilevers With Interferometric Bragg Grating Interrogation

Lewis G. Carpenter, Christopher Holmes, Benjamin D. Snow, James C. Gates, and Peter G. R. Smith

Optoelectronic Research Centre, University of Southampton, Southampton SO17 1BJ, U.K.

DOI: 10.1109/JPHOT.2012.2210396

Manuscript received June 14, 2012; revised July 18, 2012; accepted July 21, 2012. Date of current version August 2, 2012. Corresponding author: L. G. Carpenter (e-mail: lc906@orc.soton.ac.uk).

Abstract: Germanosilicate glass microcantilevers are fabricated featuring an integrated Fabry–Pérot interferometer. Direct UV writing of single-mode planar waveguides and Bragg gratings is combined with physical micromachining, using a precision dicing saw, to realize glass microcantilevers on a silicon platform. The device presented here has a wavelength shift force sensitivity of 330 nm/N, which is calibrated using a surface profilometer measurement and is an order of magnitude better than current state-of-the-art Bragg-grating-based sensors. The device also shows an approximately tenfold increase in amplitude modulation compared with a similar device architecture utilizing a single Gaussian-apodized Bragg grating. By forming the Fabry–Pérot cavity around the point of greatest strain, we reduce the unwanted effects of grating chirp as the cantilever is deflected and relate the performance to a mechanical model that relates cavity phase shift to deflection.

Index Terms: Micro and nano opto-electro-mechanical systems (MOEMS), sensors, waveguide devices.

1. Introduction

Microcantilever structures have proven useful for miniaturized sensing devices with applications ranging from detection of chemical and biological analytes to sensing changes in the physical environment. Cantilever deflection is commonly sensed by either electronic or optical means. While electronic detection is most common (e.g., MEMS), optical approaches are also widely used; these include free-space optics, e.g., atomic force microscopy (AFM) and waveguide-based sensors [1]–[3]. Both electronic and optical cantilever deflection interrogation methods have associated benefits and limitations. Electronic interrogation is cost effective and well established; however, it cannot be used in areas of strong EM fields or in hazardous environments where there are ignition risks. Conversely, fiber optic interrogation can work in extreme environments and can be used over large distances for undersea hydrophone systems [4]. A general weakness with optical sensor systems employing free-space components is alignment and stability [3]. Waveguide-based cantilever devices offer the high sensitivity of free-space optics but without the regular need for realignment; such devices are regularly reported using fibers. Bragg gratings are often inscribed in fibers to allow deflection detection, but the sizes of these cantilevers are typically on the scale of centimeters [5]. A micrometer-scale fiber-based design, where cantilevers are fabricated from the facet of the fiber, has been shown to achieve sensitivities comparable to those of commercially available instruments [6]. While fibers are an attractive route for single-cantilever devices, it is difficult to have multiple

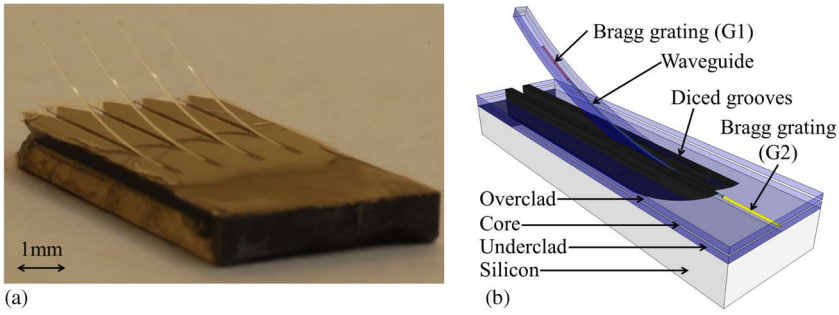

Fig. 1. a) Photograph of glass microcantilevers on integrated optic chip. b) Schematic of Fabry–Pérot glass microcantilever, showing the location of channel waveguide, Bragg gratings, and precision diced grooves (not to scale).

cantilever components integrated on a single device. Integrated optics offers a route to realize multiple cantilevers on a single chip.

Our approach to creating silica-on-silicon-chip-based germanosilicate glass microcantilevers [7] is based on a combination of direct UV writing, precision physical micromachining, wet etching, and yield devices, as seen in Fig. 1(a). These glass cantilevers combine integrated optics within a micrometer-scale beam creating a microoptomechanical system (MOMS). These techniques allow rapid prototyping of silica MOMS cantilevers with a variety of lengths and widths integrated with single-mode low-loss waveguides and Bragg gratings within the telecommunications C-band (1525–1565 nm) [7].

In previous work, we reported optical measurements of single Bragg gratings to interrogate the cantilever's mechanical damping coefficient [7]; this paper focuses on Fabry–Pérot cantilever interrogation. This device takes advantage of spectrally matched Bragg gratings within the bulk chip and cantilever to form a Fabry–Pérot interferometer. An induced deflection of the cantilever will result in a linear strain along its length. By incorporating a waveguide within the cantilever, an optical phase change occurs upon strain. In this instance, phase change is sensed interferometrically between a pair of Bragg gratings G1 and G2, allowing the mechanical flexure of the cantilever to be investigated. This is illustrated schematically in Fig. 1(b), where Bragg grating G1 resides in the cantilever, and Bragg grating G2 is within the bulk chip.

In order to develop understanding of these devices, it is necessary to investigate both the structural mechanics of the microcantilevers and interactions of the strain field with the optical phase-shift properties that determine the Fabry–Pérot response. Within this work, coupled-mode theory (CMT) is used to fit the spectral response of the Bragg grating cavity when subjected to an applied point force along the cantilever. The reason for using CMT is that it fully describes the spectral features caused by the complicated interplay between the Bragg grating Fabry–Pérot and the cantilever geometry. By creating a Fabry–Pérot structure, we take advantage of sharp spectral fringes that can be achieved when high-reflectivity reflectors are used, i.e., saturated Bragg gratings. By separating the two reflectors into regions over which the strain is homogeneous [see Fig. 1(b)] and locating them in the free cantilever (G1) and in the substrate (G2), we retain the sensitivity to strain at the pivot point of the cantilever while simultaneously achieving a sharp spectral response. The alternative route to create a sharply changing spectral reflectivity (i.e., a long grating) to improve sensitivity is not appropriate as the inhomogeneous strain along the grating creates chirp and distorts the spectrum under load.

This paper focuses on the optical characterization, deflection testing, and the modeling of the Fabry–Pérot cantilever's strain response. First, the operational principle and mechanical theory relating point strain to Fabry–Pérot phase shift is proposed. Optical characterization included preparatory work to determine the spectral shift associated with the fabrication process and the resultant Fabry–Pérot spectra. The Fabry–Pérot device is then subjected to a point force by means of a surface profiler and its spectra recorded as the cantilever is deflected. Benefits of a cavity versus single Bragg grating for single-wavelength intensity interrogation are discussed. The Fabry–Pérot fringe shift from applied strain is measured, and CMT is utilized to fit to the comb's spectral

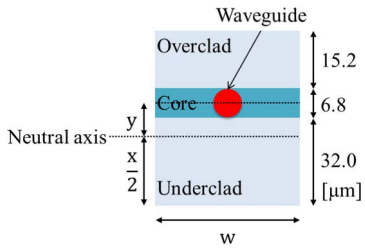

Fig. 2. Cantilever glass layer dimensions and composition (not to scale).

characteristics with strain. The CMT produces an optical phase shift for the unstrained and strained states of the cantilever. The paper concludes with comments on the device's signal-to-noise ratio and sensitivity.

2. Operational Principle

Standard theory for the strain in a bending cantilever can be applied to predict the optical phase of the Fabry–Pérot. The cantilever is assumed to be a homogenous isotropic rectangular beam, and its response to strain is related to its second moment of inertia. Standard derivation yields a simplified expression relating force to strain (1) [8],

$$\varepsilon = \frac{12Fly}{Ewx^3} \tag{1}$$

where F is the force on the cantilever, l is the length of the cantilever, y is the distance of the waveguide from the neutral axis, E is Young's modulus, w is the cantilever's width, and x is the thickness of the cantilever. As will be described later in Section 3.2, we used a surface profilometer to calibrate the mechanical properties and relate to the optical response. Using appropriate values, we can calculate the expected strain for an applied force, and in the following calculation, the values for the maximum experimental deflection (described in Section 3.2) are used. The cantilever and experimental parameters are as follows: 491 μN of force (F) over a cantilever length (l) of 4.1 mm, a vertical displacement from the neutral axis (y) of 8 μm as measured from the waveguide, a Young's modulus (E) of 80 GPa for PECVD silica [9], a cantilever width (w) of 73 μm, and a thickness (x) of 54 μm (see Fig. 2). From this equation, the strain at the pivot point, which is the point of maximum strain where the cantilever joins the chip, is calculated to be 219 $\mu\varepsilon$ (microstrain).

It is useful to treat the two physical mechanisms that cause the FP fringe shift independently. The two mechanisms are the change in cavity length as the cantilever deflects downwards and the change in the refractive index of the silica waveguide due to the strain-optic effect. A linear approximation was used for strain along the length of the cantilever; the approximation was calculated from the pivot point to the end of the stylus sweep (4.1 mm along the cantilever). The length of the cavity in the cantilever affected by strain (L') was measured to be 1.8 mm. The length of the cavity (L') is the distance measured from the pivot point (i.e., the point where the cantilever becomes free from the substrate) to the middle of the Bragg grating within the cantilever, corresponding to an effective reflection point (approximated to be at the midpoint of the grating), L' can been seen in Fig. 4. The location of the pivot point of the microcantilever was identified by imaging using a white light interferometer (Zemetrics Zescope). The phase change within the Fabry–Pérot will be the integrated optical path change due to the strain along its length, under the linear assumption that the average strain applied to the Fabry–Pérot is given by the midpoint of the cavity within the cantilever. The average applied strain (ε_{ave}) for this cavity length is 172 $\mu\varepsilon$. The total induced optical change in phase $(\Delta\varphi)$ for a single round trip caused by this strain is given by (2) [10],

$$\Delta\varphi = \left\{\frac{2\pi n_{eff}}{\lambda_o}\right\}\left\{1 - \frac{n_{eff}^2}{2}[p_{12} - \upsilon(p_{11} + p_{12})]\right\}L'\varepsilon_{ave} \tag{2}$$

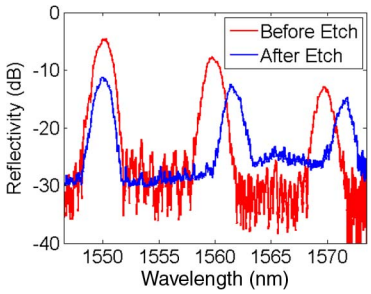

Fig. 3. Reflection spectra of the three 1-mm Gaussian-apodized Bragg gratings before and after wet etching, TE polarization. The Bragg grating centered at 1550 nm is in the bulk chip, and the other two are located within the cantilever.

where $\Delta\varphi$ is the phase difference, n_{eff} is the effective refractive index of the waveguide, λ_o is the central wavelength of the comb, p_{ij} is the strain-optic tensor, υ is Poisson's ratio, L' is the length of the cavity affected by strain, and ε_{ave} is the average induced strain. With a n_{eff} of 1.448, λ_o is taken as $\sim$1550.4 nm from Fig. 5, taking the values for PECVD silica of p_{11} of 0.121, p_{12} of 0.270, υ of 0.2 [9], a value for L' of 1.8 mm, and strain ε_{ave} of 172 $\mu\varepsilon$. This yields a predicted $\Delta\varphi$ of 1.42 radians. This theoretical prediction will be compared in Section 3.3 with experimental spectral data, where CMT is used to relate the observed Fabry–Pérot fringe shift.

3. Experimental Results

3.1. Fabry–Pérot Germanosilicate Glass Microcantilever Fabrication

Prior work by our group has reported the fabrication and characterization of an integrated microcantilever making use of a single Bragg grating; similar fabrication techniques have been used here. The basic glass microcantilever fabrication route is to physically micromachine, using a dicing saw, two grooves into flame hydrolysis deposition (FHD) silica-on-silicon multilayer wafers through to the underlying silicon [see Fig. 1(b)], predefining the dimensions (length and width) of the cantilevers. Direct UV writing is used to create the waveguides and Bragg gratings into a silica ridge. The single-mode channel waveguides at 1550 nm have a n_{eff} of 1.448, a width of 6 μm defined by the UV laser spot size, and a height of 6.8 μm as defined by the planar layer of the substrate [11], [12]. Bragg gratings are inscribed using two beam interference and with amplitude modulation of the UV laser beam, simultaneously with waveguide definition. Index contrasts of 0.001 are typically achieved, and Gaussian apodization is implemented with amplitude modulation in a Gaussian intensity; this suppresses the sidelobes of a uniform Bragg grating. After which, the microcantilevers are released from the silicon substrate with potassium hydroxide etchant (KOH) [7].

In our device, the Bragg gratings making the Fabry–Pérot are located within the cantilever (G1) and the bulk chip (G2), as shown in Fig. 1(b). We have found experimentally that G1 experiences a central Bragg wavelength shift of 1.77 nm for the TE polarization after the KOH etching process. The spectral shift of the Bragg grating residing in the cantilever results from the release of compressive stress as a consequence of high consolidation temperatures ($\sim$1200 °C) used in FHD and the mismatch in thermal expansion coefficients between the silica and silicon. To ensure the reflection bands of the two gratings should (approximately) overlap, the shift was empirically found for the particular wafer. The spectral shift was found by creating a device with three 1-mm Gaussian-apodized gratings, two residing within the cantilever and one within the chip. The reflection spectra were collected before and after wet etching with KOH, as shown in Fig. 3; a broadband source, circulator, polarizer, and an optical spectrum analyzer (OSA) were used for spectra collection. The TE reflection spectra data show an average spectral shift in central wavelength of 1.77 nm.

Knowing the expected wavelength shift, a new substrate containing micromachined grooves was used to fabricate a Fabry–Pérot device with the Bragg grating in the cantilever (G1) spectrally

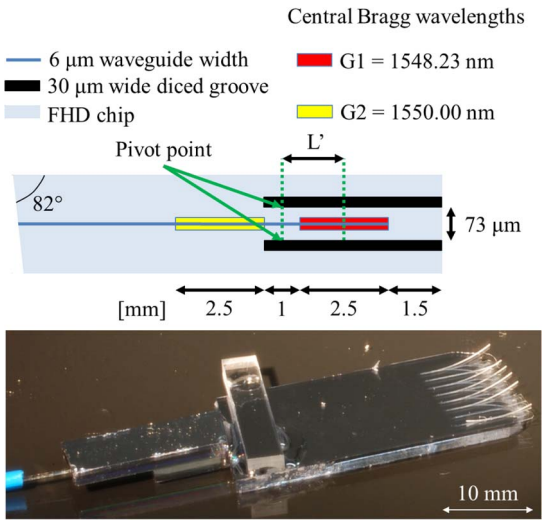

Fig. 4. (Above) Plan view of device in Fig. 1(b). (Below) Photograph of the actual device coupled with a polarizing maintaining fiber and pigtail; transparent UV-cured gluing is used for adhesion.

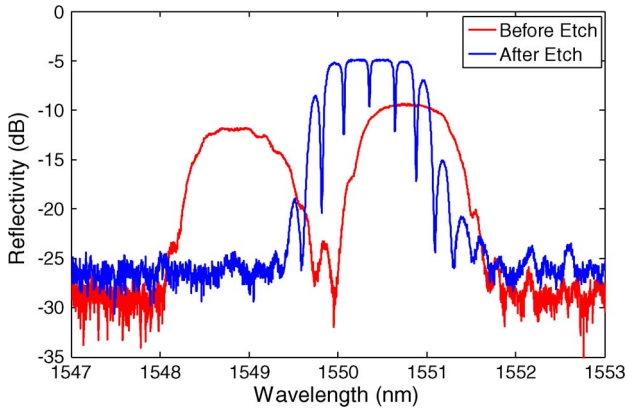

Fig. 5. Reflection spectra of the device, before and after wet etching, TE polarization. The two gratings are spectrally displaced by 1.77 nm for the TE polarization before etching and overlay successfully after etching.

shifted by −1.77 nm compared with that in the bulk (G2). This ensured spectral overlap of the two gratings after etching. The schematic of this Fabry–Pérot cantilever structure is shown in Fig. 4. As can be seen in Fig. 4, only G1 and the space between the gratings will be sensitive to strain; G2 will be insensitive to strain by being placed in the chip.

Fig. 4 shows the location and initial wavelengths of the Bragg gratings before etching, the G1 (red) and G2 (yellow) gratings forming the Fabry–Pérot after cantilever release. The microcantilever is formed between the pair of micromachined grooves (black areas). To minimize optical backscatter and improve return loss, the MOMS device had an input facet diced to 8°; this ensures any Fresnel reflections are reflected away from the waveguide. To further reduce return loss, the waveguide in the cantilever was also terminated 1.5 mm from the end to allow light to diffuse into the planar layer and reduces back-reflection from the cantilever facet. To optically characterize the Fabry–Pérot microcantilever, the reflection spectra were collected using a broadband source, OSA, circulator, and polarizer such that TE and TM transmission spectra could be individually interrogated. The spectra were taken before and after wet etching of the device, as shown in Fig. 5. The figure shows the initial spectral separation of the two cavity gratings and after etching the creation of the Fabry–Pérot cavity featuring sharp resonance fringes.

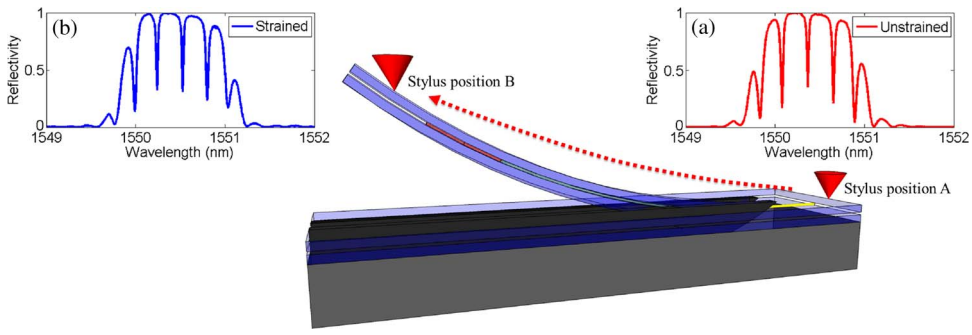

Fig. 6. Side view of the cantilever showing the progression of the stylus profiler along its length. The resultant spectra are shown for the unstrained (A) and strained (B) states.

3.2. Mechanical Characterization

To explore the overall effect of applied force to the cantilever, a surface profiling technique was used to interrogate the Fabry–Pérot cantilever [13]. A KLA Tencor P16 stylus profiler was used to apply a point force at positions ranging from the start of the cantilever to 4.1 mm along its length. The stylus profiler scan was limited to the first 4.1 mm of the 5-mm cantilever because of the limited vertical scan range of the stylus profiler. The stylus load was 491 μN, and this force was applied to the cantilever (see Fig. 6) and then raster scanned six times, moving laterally over the waveguide in 1-μm steps. A raster scan technique was used to ensure that the applied force about the pivot point had a negligible component of torsional strain. While the profiler was applying the linear strain, simultaneous reflection spectra were collected from the device using a broadband source, OSA, circulator, and polarizer set for TE. Below, a schematic is shown of the stylus progress along the cantilever.

Compared with our previous work with a single grating, the Fabry–Pérot offers sharper spectral features with greater spectral intensity/wavelength gradients and should give better sensitivity to strain. To investigate this benefit, the model and spectra reported in [7] were used, and the intensity changes due to strain were calculated. A 1-mm Gaussian-apodized Bragg grating was modeled at the point of highest strain and employed an identical cantilever geometry (i.e., same thickness, length, applied force, *etc.*) as the new Fabry–Pérot device and thus offers a reasonable comparison. This model provided both the Bragg central wavelength shift and the maximum intensity change at a single wavelength, thereby simulating the response of a fixed wavelength laser interrogation system. Comparison of the responses was undertaken for a strain of 8 $\mu\varepsilon$, which is equivalent to 23 μN of applied point load 4.1 mm along the cantilever length. The modeled shift for this force for a single Bragg grating was 11.0 pm compared with a measured shift of 10.7 pm for our new Fabry–Pérot device. Thus, both devices show similar spectral change. To simulate intensity-based interrogation, a single wavelength was monitored at a point of highest gradient for both the Fabry–Pérot comb and single Bragg grating systems, and the relative intensity changes were determined. However, even though the wavelength shift was comparable for the cavity device, there was a factor of 11 times improvement in the intensity modulation compared with that of the single Bragg grating device. This 11-fold improvement can be attributed to the sharpness of the Fabry–Pérot fringes compared with a simple Bragg grating giving much greater intensity modulation even though the spectral shift is comparable. The fitting of the Fabry–Pérot comb shift with applied point force using CMT is discussed below.

3.3. CMT Fitting

CMT [14] was utilized to fit the comb and infer how the phase between the Bragg gratings, forming the Fabry–Pérot, changed with applied stylus force. CMT was used as it can encompass several Bragg grating and Fabry–Pérot parameters such as chirp and Fabry–Pérot spectral overlap, which are difficult to express analytically. The unstrained Fabry–Pérot spectra were fitted using

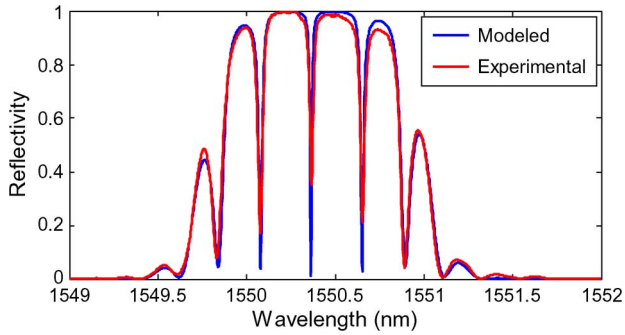

Fig. 7. Experimental and modeled reflectivity of the Fabry–Pérot (in an unstrained state).

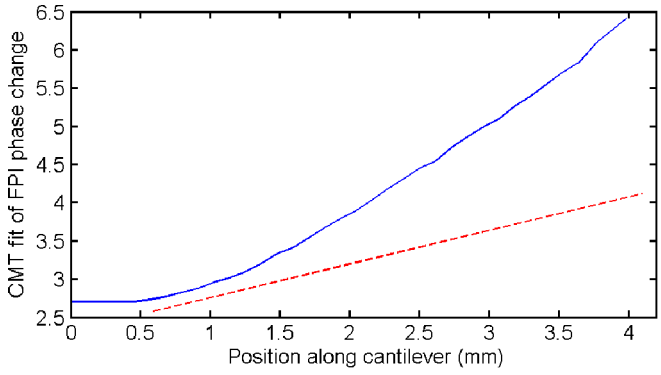

Fig. 8. Dependence of inferred phase shift from Fabry–Pérot analysis as a function of stylus position *N.B.* the stylus first makes contact with the cantilever at ~0.5 mm. The solid line is the CMT fit of phase, and the dotted line is the simple linear deflection model with a 2.70 radians offset accounting for initial starting phase.

CMT, as shown in Fig. 7. The Bragg gratings were modeled with Gaussian apodization, while a Nelder–Mead simplex search method [15] was used to optimize several of the Bragg grating parameters.

The fitted parameters included: modulation depth of the effective waveguide refractive index (Δn_{eff}), the spectral mismatch in Bragg grating central wavelength of the two gratings making up the Fabry–Pérot $(\delta\lambda)$, the phase between them equivalent to the optical path length difference (Φ), the linear chirp of the cantilever Bragg grating (F), and an amplitude offset (C). An effective refractive index of 1.448 for the waveguide was used, and a 535-nm grating period was used for the grating in the bulk as measured from Fig. 5. For the unstrained condition, the Bragg gratings had the following parameters: $\Delta n_{eff} = 8.06 \times 10^{-4}$, $\delta\lambda = -24.3$ pm, $\Phi = 2.70$ radians, $F = 1.21 \times 10^{-6}$ nm/cm, and $C = 1.35 \times 10^{-3}$. Using the same grating parameters as for the unstrained Fabry–Pérot, except for phase, the progressive increase in phase with profiler deflection was fitted, resulting in a new total phase (Φ) of 6.41 radians with a load applied at 4.1 mm. Thus, the shift between the initial starting phase (2.70 radians) to the maximum value (6.41 radians) is 3.71 radians. This should be compared with our predicted phase shift (from Section 2) of only 1.42 radians. This discrepancy will be discussed in the next section. To convert from the modeled parameter phase difference $(\Delta\varphi)$ to the fitted phase parameter (Φ), the initial phase of the Fabry–Pérot (2.70) must be added to $\Delta\varphi$.

Fig. 8 shows the dependence of the Fabry–Pérot phase shift, inferred from CMT, as a function of stylus position on the microcantilever. The trend shows a progressive increase in phase of the Fabry–Pérot; the change in phase (Φ) between the unstrained and strained Fabry–Pérot was 3.71 radians.

The 1.42 radians phase (Φ) calculated by the mechanical theory (see Section 2) and the 3.71 radians from the CMT fitted experimental data therefore disagree by a factor of $\sim$2.6. There are two mechanisms that may explain this discrepancy. The first is that our calculation assumes only small deflection, and so only predicts the initial linear deflection character, while the second is that the deflection is likely to be nonlinear for greater deflections plus is affected by both the residual stress in the glass laminate and our model ignores the complex bending at the pivot point of the cantilever where the geometry is more complicated. It is possible to use the mechanical model to predict an initial slope for the response; this is shown in Fig. 8 (dashed line), and it is clear that the initial gradient is very similar. Thus, we attribute our discrepancy to the nonlinear nature of the bending. There is also a discrepancy in the phase for small deflections; we believe this could be attributed to errors in the mechanical properties of the germanosilicate glass, i.e., Young's modulus, strain-optic tensor, and Poisson's ratio.

To quantify the minimum resolvable force, the signal-to-noise ratio of the device and interrogation equipment was examined. Unstrained Fabry–Pérot cantilever spectra were measured, and a single fringe from these data was fitted via a simple inverted Gaussian function to observe phase noise, via monitoring the central wavelength jitter of the inverted Gaussian function. The stylus profiler data were used to provide force calibration of the particular fringe observed. Based on recorded data, the resultant standard deviation of the detected wavelength shifts (due to random experimental noise) indicates that forces as small as 264 nN are potentially resolvable, which would correspond to a mass of 27 ng applied at the 4.1-mm point on the cantilever. A commonly used metric of sensitivity for grating-based actuators is wavelength shift per unit applied force. For the system presented here, the sensitivity is 330 nm/N, over 20 times more sensitive than a similar MEMS Bragg grating device albeit [16] one containing a structure featuring both ends fixed and thus offering potential for higher frequency performance. Additionally, our new structure is orders of magnitude more sensitive in terms of spectral shift per applied force than a fiber Bragg-grating-based sensor [17] although does not offer the reconfigurable inertial mass of this other work.

4. Conclusion

We have demonstrated, to our knowledge, the first MOMS device with a Bragg grating Fabry–Pérot interferometer contained within an integrated glass microcantilever. To fabricate the device, a spectral compensation technique was used to overcome stress artifacts and ensure correct spectral overlap of two *strong* Bragg gratings and thus achieve Fabry–Pérot interference. CMT allowed fitting of the spectra and allows full consideration of the *strong* nature of the Bragg gratings. A mechanical model using appropriate bending theory and strain-optic factors allows a prediction of the expected phase shift in the Fabry–Pérot response under load. To confirm the validity of the model, experiments were undertaken to investigate the optical response and compare it to mechanical measurements made using a commercial stylus profiler. The actual cantilever showed greater phase shift than our simple predicted, and we attribute this to nonlinear bending at larger deflections. The finesse of the Fabry–Pérot yields a factor of 11 improvement for an intensity-based measurement compared with a similar device utilizing a single Gaussian-apodized Bragg grating. A maximum phase shift of the Fabry–Pérot interferometer (3.71 radians) was recorded for a 491-μN applied force at the end of the cantilever. Data analysis also showed the smallest resolvable force of the device is 264 nN with a wavelength shift force sensitivity of 330 nm/N, an order of magnitude larger than previously reported, and demonstrating clearly the benefits of using a Fabry–Pérot structure.

References

[1] K. M. Goeders, J. S. Colton, and L. A. Bottomley, "Microcantilevers: Sensing chemical interactions via mechanical motion," *Chem. Rev.*, vol. 108, no. 2, pp. 522–542, Feb. 2008.

[2] A. Llobera, V. J. Cadarso, K. Zinoviev, C. Dominguez, S. Buttgenbach, J. Vila, J. A. Plaza, and S. Biittgenbach, "Poly(Dimethylsiloxane) waveguide cantilevers for optomechanical sensing," *IEEE Photon. Technol. Lett.*, vol. 21, no. 2, pp. 79–81, Jan. 2009.

[3] R. G. Hunsperger, *Integrated Optics Theory and Technology,* 6th ed. New York: Springer-Verlag, 2009.
[4] C. K. Kirkendall and A. Dandridge, "Overview of high performance fibre-optic sensing," *J. Phys. D, Appl. Phys.*, vol. 37, no. 18, pp. R197–R216, Sep. 2004.
[5] K.-R. Sohn and J.-H. Shim, "Liquid-level monitoring sensor systems using fiber Bragg grating embedded in cantilever," *Sens. Actuators A, Phys*., vol. 152, no. 2, pp. 248–251, Jun. 2009.
[6] D. Iannuzzi, K. Heeck, M. Slaman, S. de Man, J. H. Rector, H. Schreuders, J. W. Berenschot, V. J. Gadgil, R. G. P. Sanders, M. C. Elwenspoek, and S. Deladi, "Fibre-top cantilevers: Design, fabrication and applications," *Meas. Sci. Technol.*, vol. 18, no. 10, pp. 3247–3252, Oct. 2007.
[7] L. G. Carpenter, C. Holmes, H. L. Rogers, P. G. R. Smith, and J. C. Gates, "Integrated optic glass microcantilevers with Bragg grating interrogation," *Opt. Exp.*, vol. 18, no. 22, pp. 23 296–23 301, Oct. 2010.
[8] J. M. Gere and S. P. Timoshenko, *Mechanics of Materials*, 4th ed. Gloucestershire, U.K.: Stanley Thornes Ltd., 1999.
[9] L. Grave De Peralta, A. A. Bernussi, H. Temkin, M. M. Borhani, and D. E. Doucette, "Silicon-dioxide waveguides with low birefringence," *IEEE J. Quantum Electron.*, vol. 39, no. 7, pp. 874–879, Jul. 2003.
[10] Springer Handbook of Experimental Solid Mechanics, W. N. Sharpe, Jr., Ed. New York: Springer-Verlag, 2008.
[11] M. Svalgaard, C. V. Poulsen, A. Bjarklev, and O. Poulsen, "Direct UV writing of buried singlemode channel waveguides in Ge-doped silica films," *Electron. Lett.*, vol. 30, no. 17, pp. 1401–1403, Aug. 1994.
[12] G. D. Emmerson, C. B. E. Gawith, S. P. Watts, R. B. Williams, P. G. R. Smith, S. G. McMeekin, J. R. Bonar, and R. I. Laming, "All-UV-written integrated planar Bragg gratings and channel waveguides through single-step direct grating writing," *Proc. Inst. Elect. Eng.—Optoelectron.*, vol. 151, no. 2, pp. 119–122, Apr. 2004.
[13] C. Holmes, L. G. Carpenter, H. L. Rogers, J. C. Gates, and P. G. R. Smith, "Physical sensitivity of silica micro-cantilevers fabricated using direct UV writing and micromachining," in *Proc. 11th Int. Symp. LPM*, Stuttgart, Germany, 2010.
[14] T. Erdogan, "Fiber grating spectra," *J. Lightw. Technol.*, vol. 15, no. 8, pp. 1277–1294, Aug. 1997.
[15] J. C. Lagarias, J. A. Reeds, M. H. Wright, and P. E. Wright, "Convergence properties of the Nelder–Mead simplex method in low dimensions," *SIAM J. Optim.*, vol. 9, no. 1, pp. 112–147, 1998.
[16] K. Reck, E. V. Thomsen, and O. Hansen, "MEMS Bragg grating force sensor," *Opt. Exp.*, vol. 19, no. 20, pp. 19190–19198, Sep. 2011.
[17] N. Basumallick, I. Chatterjee, P. Biswas, K. Dasgupta, and S. Bandyopadhyay, "Fiber Bragg grating accelerometer with enhanced sensitivity," *Sens. Actuators A, Phys.*, vol. 173, no. 1, pp. 108–115, Jan. 2012.